Composites: Part A 173 (2023) 107701

Contents lists available at ScienceDirect

Composites Part A

journal homepage: www.elsevier.com/locate/compositesa

Mechanical and piezoresistive behavior of selectively laser sintered MWCNT/UHMWPE nanocomposites

Muhammad Umar Azam [a], Andreas Schiffer [a,*], S Kumar [b,*]

[a] Department of Mechanical Engineering, Khalifa University, P.O. Box 127788, Abu Dhabi, United Arab Emirates
[b] James Watt School of Engineering, University of Glasgow, Glasgow G12 8QQ, UK

ARTICLE INFO

Keywords:
3D printing
Sintering
Strain sensing
Polymer-matrix composites (PMCs)

ABSTRACT

Herein, we present the mechanical and piezoresistive behavior of MWCNT/UHMWPE nanocomposites processed via selective laser sintering (SLS) under tensile, flexural and cyclic loadings. We show that the uniform dispersion of MWCNTs in UHMWPE enhances crystallinity (+10% for 0.5 wt% MWCNT) and decreases porosity (as evidenced by μCT images), evincing the lowest porosity (~1%) and the highest tensile strength of 20.3 MPa which is ~ 45% higher than the maximum tensile strength of extant SLS processed UHMWPE and UHMWPE-based composites. The nanocomposite also exhibits superior piezoresistive characteristics, showing a sensitivity factor (in tension) of 0.6 and 2.6 in the elastic and inelastic regime, respectively. Furthermore, 2D-hexagonal nanocomposite lattices with a relative density of 50% reveal a linear piezoresistive response with a gauge factor of 1 and show consistent and stable strain sensing capability over 100 repeated load cycles. The results demonstrate the potential of MWCNT/UHMWPE nanocomposites for the development of smart biomedical devices.

1. Introduction

Over the last two decades, additive manufacturing (AM), also known as 3D printing, has opened new horizons in manufacturing, offering several unique benefits, such as a high degree of design flexibility and the ability to fabricate complex geometries with good dimensional accuracy and low wastage of materials. Further, AM enables the fabrication of structural components with functionalities such as self-healing, self-healing or morphing, in a single step without the need of any post-processing steps (e.g. machining etc.) [1, 2].

Among various AM techniques, selective laser sintering (SLS) being one of the four powder-bed fusion processes, exhibits various advantages such as relatively high strength of the printed parts, the absence of support structures, as well as the ability to produce large batches and to recycle unfused powder [3]. In this technique, powder particles are spread over the print bed through a roller and are selectively sintered together inside an enclosed chamber using a laser source. This process is then repeated layer-upon-layer until the final product is realized. Although SLS offers several advantages, there are practical limitations in the choice of feedstock polymers because the process relies upon complex diffusional processes across length scales requiring a specific set of thermomechanical and thermophysical properties [4].

Ultra-high molecular weight polyethylene (UHMWPE) is a semi-crystalline thermoplastic polymer, possessing extraordinary characteristics such as good lubricity, high abrasion and impact resistance, chemical inertness against many acids and alkalis, thermal stability and biocompatibility [5, 6]. Due to these excellent mechanical and physical properties, UHMWPE has found many practical applications in various fields, including transportation, machineries, textiles and sports equipment [6]. Most importantly, UHMWPE is extensively being used in biomedical applications for artificial joints and orthopedic implants, and has contributed to the success of total knee arthroplasty (TKA) and total hip arthroplasty (THA) [7]. On the other hand, the use of UHMWPE in orthopedic implants has some drawbacks since the wear debris from the implant can cause local reaction leading to osteolysis [8, 9]. Furthermore, there are some limitations regarding the processing of UHMWPE due to its higher molecular weight and melt viscosity, rendering extrusion-based processing difficult [10]. The major difficulties in processing UHMWPE via SLS are hard caking of the powder bed and curling/sliding of the sintered part during printing [11] which can lead to failed prints. These issues are related to the narrow window of SLS-process parameters for UHMWPE due to which its potential in 3D

* Corresponding authors.
E-mail addresses: andreas.schiffer@ku.ac.ae (A. Schiffer), msv.kumar@glasgow.ac.uk (S. Kumar).

https://doi.org/10.1016/j.compositesa.2023.107701
Received 28 March 2023; Received in revised form 27 June 2023; Accepted 18 July 2023
Available online 24 July 2023

printing applications has not been fully tapped.

Only a few reports of SLS 3D printed UHMWPE are currently available in the literature. Early studies in this field date back to Rimell et al. [12] who used a non-commercial SLS machine to print simple linear geometries from UHMWPE powder. However, they were unable to print sheet-like geometries due to high porosity and shrinkage of the printed parts. Later, Goodridge et al. [13] optimized the SLS-processing parameters (i.e, laser power, bed temperature etc.) and printed UHMWPE specimens for tensile and flexural testing, which showed relatively poor mechanical properties. They noted that very precise sintering parameters were required to print UHMWPE due to its narrow processing window. Khalil et al. [14–16] studied the effect of laser power on the tensile and flexural properties of UHMWPE processed via SLS. They found improvement in the parts' tensile strength and density by increasing the laser power but at the expense of the parts' dimensional accuracy. In an attempt to enhance the mechanical properties of laser-sintered UHMWPE, Song et al. [7] performed post-heat treatments on tibial inserts processed via SLS, which was shown to increase the tensile strength of the printed parts from 14.1 MPa to 24.1 MPa. Recently, Zhu et al. [11] used anti-caking agent (fumed silica) to aid the processing of UHMWPE via SLS. While the addition of fumed silica reduced the extent of caking, it also deteriorated the mechanical properties of the 3D printed parts.

In the recent years, AM has emerged as a versatile technique for fabricating electrically conductive polymer-based nanocomposites capable of exhibiting piezoresistive response [1]. Such an attribute enables *in situ* monitoring of the deformation/damage induced in a load-carrying component in service (e.g. orthopedic implant). Among various conductive nanofillers, carbonaceous fillers such as CNTs possess high strength (~1–10 GPa) and modulus (~1.0 TPa), as well as excellent thermal (3000–6000 W/m K) and electrical conductivity (10^4–10^6 S/cm) [17, 18]. Due to high aspect ratio of CNTs, conductive network can be established in the polymer matrix even at low electrical percolation thresholds [19]. However, uniform dispersion of the CNTs in the polymer matrix remains a major challenge. Although the fabrication of polymer-based nanocomposites via SLS has been the topic of recent investigations [20–26], studies on SLS 3D printing of UHMWPE-based nanocomposites with multifunctional attributes are currently lacking.

Due to processing challenges associated with narrow sintering window and high molecular weight and melt viscosity of UHMWPE, there have so far only been limited attempts to additively manufacture UHMWPE. To the best of our knowledge, this study is the first to report the successful fabrication of multi-walled carbon nanotubes (MWCNTs) incorporated UHMWPE nanocomposites via SLS technique and evaluate their mechanical and piezoresistive characteristics. These AM-enabled multi-functional UHMWPE-based nanocomposites hold promise for applications in an array of patient-specific smart orthopedic implants and devices. Initially, MWCNT/UHMWPE composite powders with 0.3, 0.5 and 1.0 wt% CNT loading were prepared via ball milling, and were then used to fabricate electrically conductive standard test specimens as well as 2D lattice structures via SLS. A large number of test prints were executed to optimize the SLS process parameters that maximize the mechanical properties of the printed parts while limiting common issues such as hard caking of the powder bed. The mechanical and piezoresistive characteristics of the 3D printed MWCNT/UHMWPE nanocomposite structures were measured under quasi-static and cyclic loading conditions, and the underlying structure-processing-property relations were discussed.

2. Experimental work

2.1. Materials

UHMWPE having a purity of 99.99% and molecular weight of $> 4.5 \times 10^6$ g/mol was procured from Nanoshel®, India. The average particle size was found to be 130 ± 33 μm via scanning electron microscopy (SEM) analysis (see Fig. 2a). PEG coated multi-walled carbon nanostructures (MWCNS) consisting of bundles of aligned MWCNTs were procured from Applied Nanostructured Solutions LLC, USA. Further details on these MWCNTs can be found in our previous studies [27,28].

2.2. Preparation of nanocomposite feedstock

The nanocomposite powders were prepared via low-energy ball milling (Pulverisette 5, Fritsch, Germany) at 200 rpm for 45 min with a ball to powder ratio of 10:1. Steel jars and steel balls were used in all experiments (Fig. 1a). Weighted amounts of MWCNTs were added to the pure UHMWPE powder to obtain nanocomposite powders with 0.3, 0.5 and 1.0 wt% MWCNT loading, which are referred to as U-0.3, U-0.5 and U-1, respectively. Additionally, U-0* represents the ball-milled pure UHMWPE powder. To ensure uniformity in the properties of all prints, the powders were artificially aged as recommended in literature [3].

2.3. 3D printing via selected laser sintering

All samples were printed flat in z-build direction using a Sharebot SnowWhite (Italy) SLS 3D printer equipped with a CO_2 laser (Fig. 1b). Note that the geometric details of samples are discussed in Section 2.5. Several test prints were executed in which we observed common issues associated with SLS of UHMWPE, such as warping and caking of the samples, as described in Section 1, Supplementary Information.. The optimal processing parameters were identified for each powder composition, as listed in Table S1 to eliminate these issues. For example, the powders with higher MWCNT loading were sintered at relatively lower bed temperature to avoid caking because MWCNTs increase the thermal conductivity of the powder due to their higher laser power absorption [29]. Furthermore, the powder feedstock was pre-heated for an hour to avoid warpage, as suggested elsewhere [10].

2.4. Characterization of feedstock and 3D printed samples

2.4.1. Scanning electron microscopy (SEM)

A high-resolution scanning electron microscope (FEI Nova NanoSEM 650) was used to examine the morphologies of the powder particles and cryogenically fractured surfaces of the printed parts. To avoid charging effects, a gold coating of thickness ≈ 10 nm was deposited on all samples prior to the SEM analysis using a sputter coater (JEC-3000FC, JEOL).

2.4.2. Micro-computed tomography (μCT)

Micro- and meso-scale pores and defects in the 3D printed specimens were analysed using a Phoenix nanotom® M nanoCT 3D scanner (GE Sensing & Inspection Technologies GmbH) which has a maximum resolution of 5 μm/voxel. All scans were taken at a resolution of 15 μm/voxel.

2.4.3. Differential scanning calorimetry (DSC)

A DSC analysis (DSC131 EVO, Setaram Instrumentation) was carried out on the nanocomposite powders to examine their thermal properties, such as melting and crystallization temperatures as well as melting enthalpies. All the powder samples were placed in Aluminum crucibles and tested between 25 °C and 200 °C with the same heating/cooling rate of 10 °C /min in N_2 environment. The crystallinity percentage (X) was calculated as follows:

$$X = \frac{\Delta H_m}{H_{100}} \cdot 100 \quad (1)$$

where ΔH_m is the melting enthalpy of the tested sample, and ΔH_{100} is the enthalpy of fusion of 100% crystalline UHMWPE (289 J/g according to [9]).

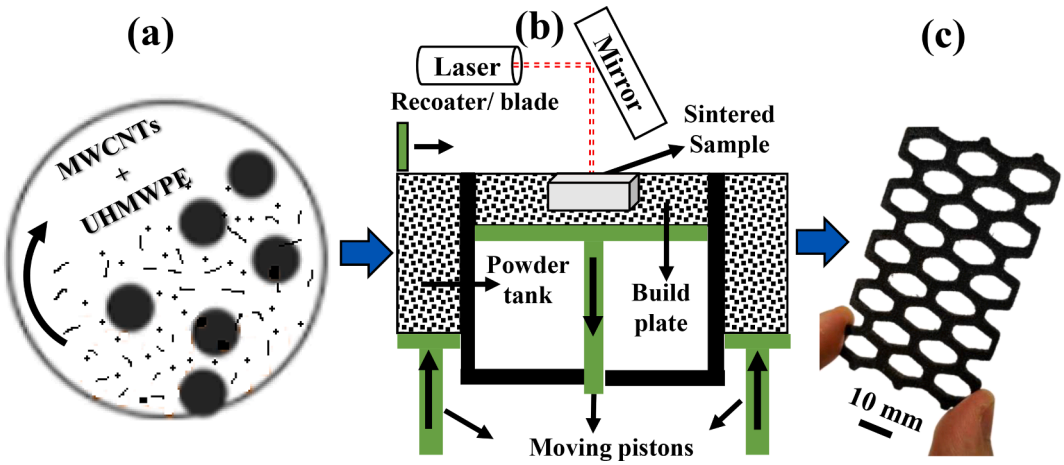

Fig. 1. Schematic of steps involved in processing of MWCNT/UHMWPE nanocomposites via SLS: (a) preparation of nanocomposite powders via ball milling, (b) 3D printing via SLS, (c) 3D printed 2D lattice structure.

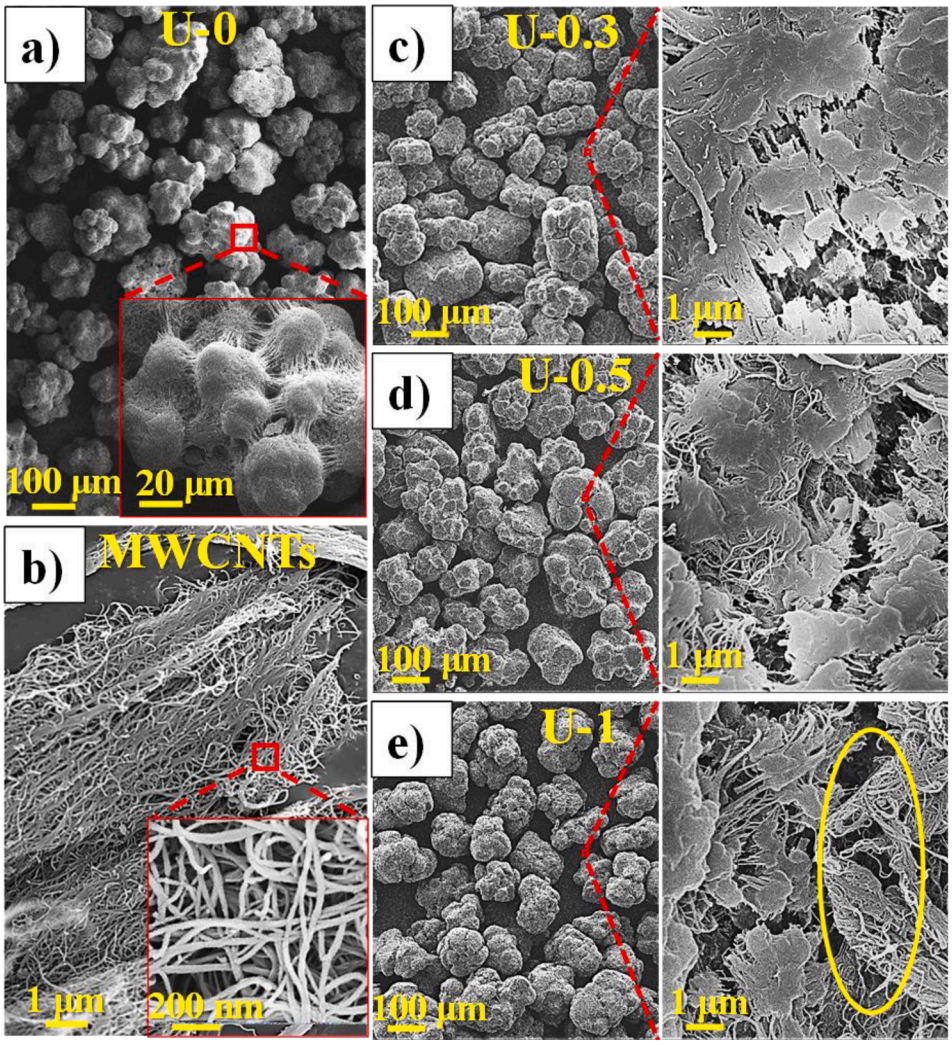

Fig. 2. SEM characterization of (a) as-received UHMWPE powder, (b) as-received MWCNTs, (c-e) ball-milled MWCNT/UHMWPE powders; the insets are magnified images.

2.4.4. Thermogravimetric analysis (TGA)

TGA analysis (SDT-Q600, TA Instruments) was performed to determine the thermal stability of the samples in terms of thermal degradation temperatures, T_d, and weight loss percentages. The TGA analysis was carried on powder feedstock in N_2 environment over a temperature range of 25–600 °C using Aluminum crucibles. A heating rate of 10 °C/min was used in all experiments. Note that T_d was chosen as the point of intersection of two tangents constructed at the starting and completion

onsets, respectively.

2.5. Mechanical testing

2.5.1. Quasi-static tensile tests

Quasi-static tensile tests were performed on dogbone-shaped specimens using a Zwick-Roell (Z005) universal testing machine (UTM) equipped with a 2.5 kN load cell. The dogbone specimens had a gauge section measuring $35 \times 5 \times 2$ mm^3 (ASTM D638 Type IV standard) and were loaded to failure at a crosshead speed of 2.5 mm/min [3]. In addition, 2D lattice structures with hexagonal unit cells (Fig. 1c) were also tested in tension using the same setup and loading speed of 2.5 mm/min. These lattice structures had a relative density (fraction of solid in a cellular structure) of 50% and were printed to a size of $77 \times 45 \times 3$ mm^3. The specimens were clamped between the grips of the UTM to obtain a gauge section of $45 \times 45 \times 3$ mm^3. The CAD model of the 2D hexagonal lattice structure with its unit cell dimensions is presented in Fig. S5 (Supplementary Information). Note that each test was repeated at least three times on identical specimens to ensure that the results are statistically consistent.

2.5.2. Repeated cyclic tests

The 3D printed 2D lattice structures with 0.5 wt% MWCNT loading were tested to assess their performance under strain-controlled cyclic loading considering the following two different test protocols:

a. *Incremental cyclic loading*: The 2D lattice structures were subjected to an incremental repeated tensile loading at a cross-head speed of 2.5 mm/min to examine the effect of plasticity/damage accumulation in the structure on the mechanical response and self-sensing characteristics. The cyclic test consisted of six stretch-release cycles with 0.25, 0.5, 1, 2, 3 and 5 % strain, respectively. In each of these stretch-release cycles, the specimens were loaded until the strain reached its maximum and then unloaded to zero stress without any holding time.
b. *Constant amplitude cyclic loading*: The sample was subjected to repeated stretch-release cyclic loading over a range of $1\% \leq \varepsilon \leq 2\%$ to examine the stability of piezoresistive performance. The crosshead speed was set to 2.5 mm/min throughout the test and the specimen was subjected to a total of 100 load cycles (without holding time). Note that we decided to limit the maximum strain to 2% to avoid the occurrence of plastic deformation or failure of the structure, while the minimum strain of 1% was chosen to ensure that the induced stresses remain tensile during the test. Note that unloading to zero strain could result in compressive stresses due to the viscoelastic nature of UHMWPE.

2.5.3. Piezoresistance measurements

The change in the electrical resistance of the samples was measured *in situ* during the mechanical tests described in Sections 2.5.1 and 2.5.2. This was done using a DMM 4050 Multimeter (Tektronix, USA) whose wire connectors were clipped onto the specimens through a layer of copper foil to minimize the contact resistance, as shown in Fig. S6 (Supplementary Information). The fixtures and loading train of the UTM were well-insulated with PVC tape to avoid charge leakage. The gauge factor, k, was calculated as follows:

$$k = \frac{\Delta(\Delta R/R_0)}{\Delta \varepsilon} \tag{2}$$

where ΔR is the measured change in electrical resistance, R_0 is the initial zero-load resistance, and ε is an applied macroscopic strain.

3. Results and discussion

3.1. Morphology of the UHMWPE and MWCNT/UHMWPE powders

Fig. 2 presents SEM images of as-received UHMWPE powder and MWCNTs as well as the ball-milled nanocomposite powders. The particles of as-received UHMWPE powder (Fig. 2a) were of irregular shape and had an average size of 130 ± 33 μm. At a higher magnification (see inset in Fig. 2a), we observe agglomerates of powder particles due to the highly cohesive nature of the inter-particle contacts, signified by the fibrils. It is clearly seen that the MWCNT/UHMWPE powder particles (Fig. 2c-e) had smoother surfaces than as-received UHMWPE particles, as a consequence of repeated collision between particles occurred during ball milling, making it easier to spread uniform layers of powder on the print bed [30]. Furthermore, the SEM images show that the MWCNTs were well dispersed in the powder up to 0.5 wt% MWCNT loading (Fig. 2c-d); however, relatively large MWCNT agglomerates, similar to those observed in the as-received MWCNT nanostructure flakes (Fig. 2b), were observed at 1 wt% MWCNT loading (Fig. 2e).

3.2. Thermal behavior

Fig. S2a-b (Supplementary Information) present, respectively, the heating and cooling curves obtained from the DSC analysis of pure UHMWPE and MWCNT/UHMWPE powders; we also include in these figures the results obtained for a ball-milled pure UHMWPE powder (dashed curves). As seen from heating curves (Fig. S2a), the melting temperatures, T_m, of the powders were largely unaffected by the presence of nanofillers. Only for the U-1 sample, a slight shift in T_m to lower temperatures was observed (see Table S3, Supplementary Information). Although the observed trends in T_m guided the choice of the SLS bed temperatures, T_b, the addition of nanofillers increased the caking tendency of UHMWPE powder during SLS and therefore, the T_b values were chosen lower than what the trends in T_m would suggest. As seen from the cooling curves (Fig. S2b), the recrystallization temperatures steadily increased with increasing MWCNT loading due to nucleation sites provided by MWCNTs promoting heterogeneous nucleation (see Table S3, Supplementary Information), as observed in previous studies (see e.g. [31]), which further limited the sintering window of the UHMWPE.

Based on the DSC thermograms in Fig. S2a, we evaluated the melting enthalpies, ΔH_m, and crystallinities, X, of the feedstock powders, as listed in Table S3 (Supplementary Information). It should be noted that the ball milling did not affect the crystallinity of as received pure UHMPWE. In general, the addition of MWCNTs increased the crystallinity as compared to the pure UHMWPE powder (U-0). However, the maximum increase in X of $\sim$ 10% was reported for the composite powder with 0.5 wt% MWCNT loading relative to the U-0; at higher concentrations of MWCNT, the crystallinity dropped slightly which can be attributed to the presence of agglomerated MWCNT bundles that act as impurities and hamper the alignment of polymer chains during the crystallization process [6].

In Fig. S2c-d (Supplementary Information) we present the TGA results (in wt.%) for the pure UHMWPE, the neat MWCNTs and the MWCNT/UHMWPE composite powders, while the corresponding thermal degradation temperatures, T_d, and weight loss percentages are listed in Table S4 (see Supplementary Information). We observe a slight shift in T_d to higher temperature with increasing MWCNT loading (see Fig. S2d and Table S4), in line with previous studies [32, 33]. This can be attributed to the high thermal stability of the MWCNTs (see Fig. S2c) which hampers the movement of polymeric chains at elevated temperatures. The residual weight percentages of the tested materials at $T \approx 600\,^{\circ}$C (see Fig. S2d) scale with their nanofiller content, and are found in reasonably good agreement with their respective MWCNT weight fractions.

3.3. Mechanical and piezoresistive response of MWCNT/UHMWPE composites

The tensile stress–strain responses of 3D printed UHMWPE and MWCNT/UHMWPE nanocomposites presented in Fig. 3a, show nonlinear trends without clearly discernible yield points. These nonlinearities can be attributed to the viscoelastic behavior of the UHMWPE matrix which exhibits relatively high loss factors (tanδ) in the range of 0.08–0.09 at room temperature, as confirmed via DMA (see Fig. S3, Supplementary Information). We also observe, from Fig. 3a, an increase in both tensile strength and Young's modulus with increasing MWCNT loading. As seen from Table 1, the U-0.5 exhibited the highest tensile strength (20.3 MPa) and Young's modulus (595 MPa) which exceeded those of the pure UHMWPE (U-0) by ~ 51% and ~ 34%, respectively. At higher MWCNT loadings (i.e. 1 wt%, U-1), the modulus and strength dropped but remained above those of the pure UHMWPE (U-0). Note that these trends are similar to those observed in three-point bending experiments (presented in Section S4, Supplementary Information) and can be explained as follows. Firstly, it is has been observed in previous studies [34] that the addition of carbonaceous nanostructures to UHMWPE promotes the formation of nanofibrils that align with the stretching direction, resulting in an increased tensile strength. Note that such nanofibrils are clearly visible in the SEM images of cryogenically fractured U-0.3, U-0.5 and U-1 samples, but are less evident for the pure UHMWPE sample (U-0) (see Fig. S7, Supplementary Information). Secondly, and more importantly, we found that the addition of MWCNTs to UHMWPE reduced the porosity of the 3D printed MWCNT/UHMWPE samples due to their high and broad optical absorption spectra in the

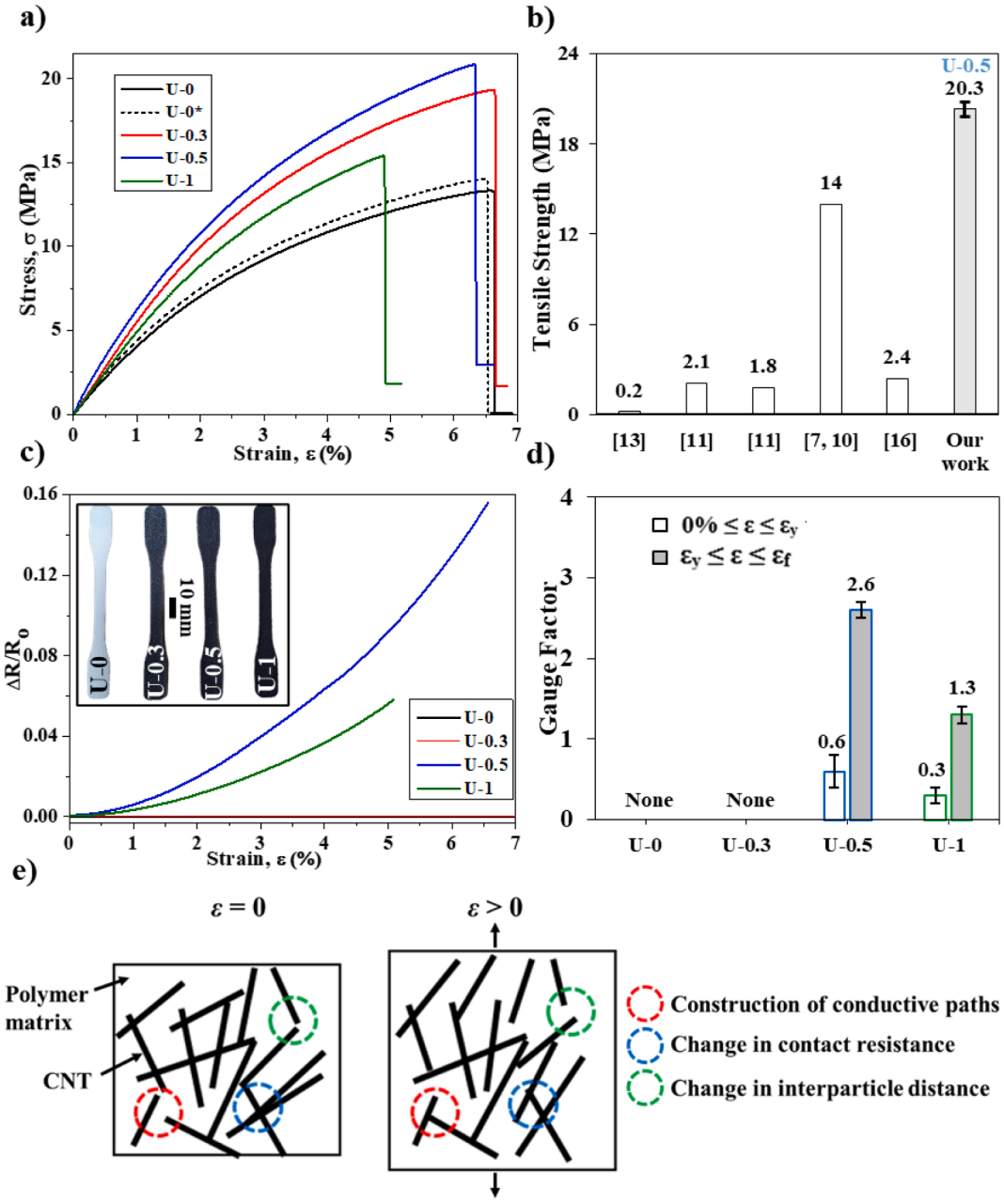

Fig. 3. Mechanical and piezoresistive behavior of pure UHMWPE and MWCNT/UHMWPE nanocomposites under uniaxial tension: (a) representative stress–strain response, (b) comparison of tensile strength of U-0.5 to similar UHMWPE-based materials reported in the literature, c) representative piezoresistive response; (d) gauge factors calculated in elastic and inelastic regimes where the error bars correspond to the standard deviation; insets are the photographs of 3D printed samples; (e) schematic of piezoresistive mechanisms in an electrically conductive CNT filled polymer nanocomposite.

Table 1
Summary of mechanical and piezoresistive characteristics of 2D lattice structures made of pure UHMWPE and MWCNT/UHMWPE nanocomposites subject to uniaxial tensile loading.

Sample ID	Tensile Strength (MPa)	Young's Modulus (MPa)	Tensile Fracture Strain (%)	Gauge factor elastic	Gauge factor inelastic	Zero-load conductivity (S/cm)
U-0	13.4 ± 0.5	444 ± 31	7 ± 0.49	–	–	–
U-0*	14 ± 0.7	460 ± 30	7 ± 0.52	–	–	–
U-0.3	19.6 ± 1	518 ± 34	7 ± 0.53	–	–	–
U-0.5	20.3 ± 0.5	595 ± 34	6.3 ± 0.5	0.6 ± 0.15	2.6 ± 0.1	3.6 ± 0.6
U-1	14.6 ± 1	510 ± 41	4.5 ± 0.3	0.3 ± 0.1	1.3 ± 0.1	256 ± 9

near-infrared regions. High optical absorption implies that MWCNTs absorb more incident light and converting absorbed light into heat. The higher thermal conductivity and laser power absorption of the MWCNTs, results in wider and deeper heat conduction, as reported in [29,35], contributing significantly to the enhancement in mechanical properties of the MWCNT/UHMWPE composites. Greater heat conduction can reduce the interspace between two successive layers, and result in the increase of the parts' density and properties. Note that, at higher concentration, MWCNTs can make processing via SLS difficult, due to increased melt viscosity and caking tendency, which impose further constraints on the maximum bed temperature and thus increases the porosity of the printed samples. Further details on the processing challenges associated with SLS of UHMWPE can be found in Section S1 (Supplementary Information) and Section 2.3. This is evident from the μCT images shown in Fig. 4 where we observe the presence of relatively large pores in the pure UHMWPE (U-0) sample, resulting in a high porosity of 15%. With the addition of MWCNTs in the range of 0.3–1 wt %, the average pore size was substantially reduced and the porosity decreased to 1–4 %. The detailed statistical analysis of porosity determined by μCT is presented in Fig. S11 (Supplementary Information). It should be mentioned that the porosity values reported in Fig. 4 only include the sintering pores and do not account for the volume fraction of larger CNT agglomerates, which are not discernable from the polymer matrix in the μCT images. The variation of the Young's modulus and tensile strength of the samples with the extent of porosity are plotted in Fig. 5, showing that the mechanical properties dropped steadily with increasing porosity. Note that the influence of porosity on mechanical properties is relatively more dominant than the reinforcing effect of the MWCNTs for the nanocomposites reported herein. This observation is further substantiated by the theoretical predictions obtained from a rule-of-mixture model for porous composites with discontinuous reinforcements, as detailed in Section S6 (Supplementary Information). Returning to Fig. 3a, we also observe that the U-1 composite failed at the lowest strain as compared to the other compositions. This can be attributed to the presence of large MWCNT agglomorates (see SEM images in Supplementary Fig. S7) which served as the starting points for damage. Furthermore, we observe, from Fig. 3a, that the ball-milled pure UHMWPE (U-0*) had a slightly higher modulus and tensile strength as compared to those of the U-0, possibly due to the favorable surface morphology of the ball-milled powder particles, as discussed in Section 3.1. By comparing the tensile strength of our 3D printed UHMWPE-based composites to those of previously reported UHMWPE and UHMWPE-based materials processed via SLS (see Fig. 3b), we found that our U-0.5 composite is the first to exceed 20 MPa in tensile strength,

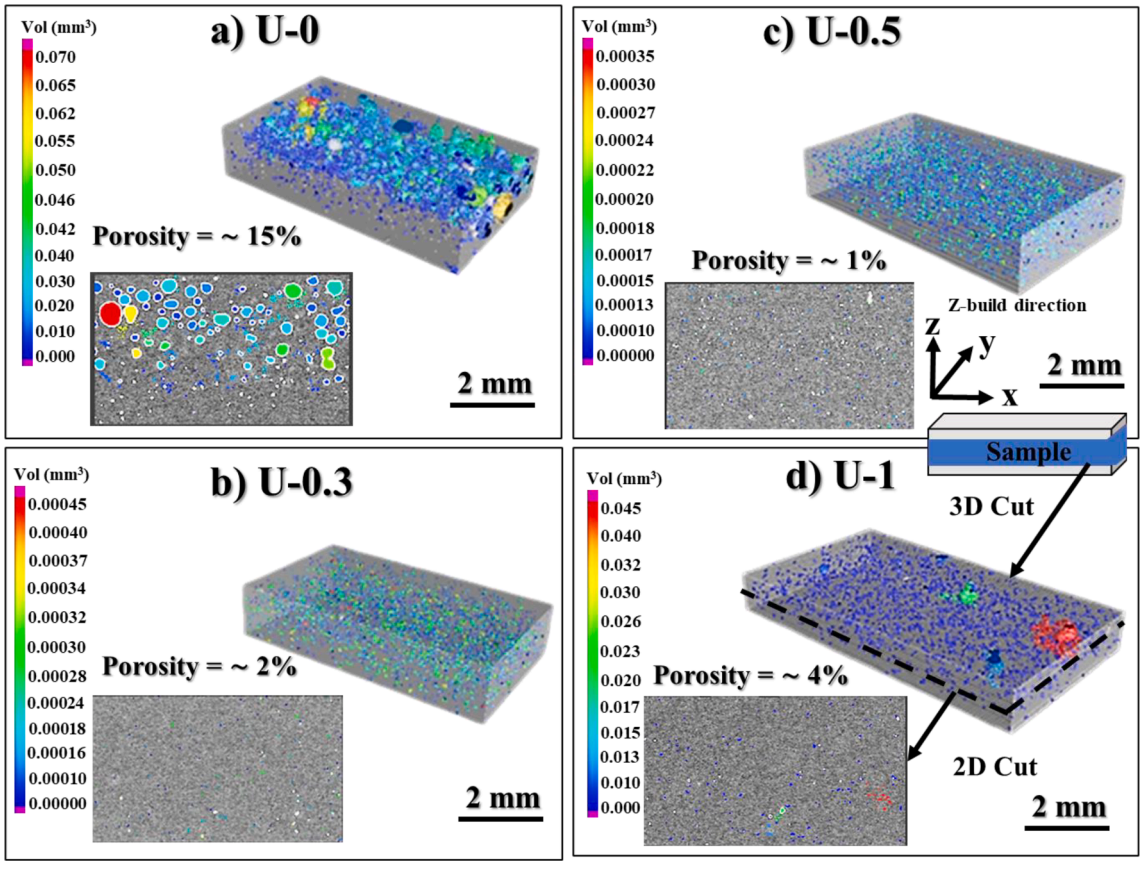

Fig. 4. μCT analysis of (a) pure UHMWPE (b) U-0.3, (c) U-0.5 and (d) U-1 samples.

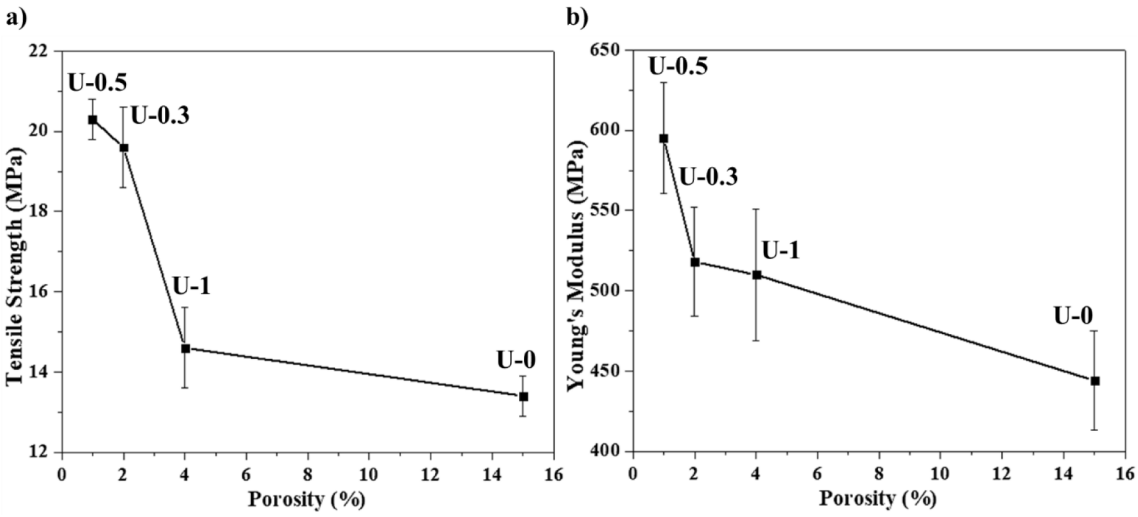

Fig. 5. Effect of porosity (measured via μCT) on (a) tensile strength and (b) Young's modulus of the 3D printed UHMWPE and MWCNT/UHMWPE composites (error bars denote standard deviations).

which is ~ 45% higher than the highest tensile strength of laser-sintered UHMWPE reported in the literature (without post-treatments).

In Fig. 3c we present the corresponding piezoresistance measurements in the form of $\Delta R/R_0$ vs. ε plots. Note that the U-0 as well as the U-0.3 samples did not show a measurable piezoresistive response as they were non-conducting, due to the absence of a percolating network of MWCNTs. Apart from the concentration of conductive filler, the percolation threshold depends on various factors such as conductivity, morphology and dispersion state of filler within the polymer matrix along with the morphology of the polymer [36, 37]. The U-0.5 and U-1 samples showed an isotropic conductivity of 3.6 ± 0.6 S/cm and 256 ± 9 S/cm, respectively, across the gauge section at zero load. The MWCNT/UHMWPE composites under tension show a positive change in normalized change in resistance (with limits being 0 and ∞). Moreover, the piezoresistance curves in Fig. 3c show nonlinear trends which become more pronounced at higher levels of strain. In polymer-based nanocomposites, the morphology of conductive network changes in response to an applied tensile load due to changes in contact resistance between MWCNTs, electron tunneling, and the destruction of conductive paths [36, 38], as illustrated in Fig. 3e. At lower strains, the piezoresistance curve is nearly linear because the change in network resistance is governed by changes in the contact resistance, while at higher strain levels, the tunneling resistance becomes more dominant, yielding nonlinear piezoresistive response concomitant with the changes in the tunneling distances [9, 36, 38, 39]. For both the U-0.5 and U-1 samples, average gauge factors were evaluated, one corresponding to the elastic regime, k_I and another one, k_{II}, over the inelastic regime (between yield and fracture strain). The yield strain, ε_y, represents a point on the stress–strain curve from where unloading to zero stress would yield a permanent strain of 0.1% [40] ($\varepsilon_y \approx 1\%$ for both U-0.5 and U-1 samples). As shown in Fig. 3d, the U-0.5 showed higher gauge factors in the elastic and inelastic regimes ($k_I = 0.6$ and $k_{II} = 2.6$) as compared to U-1 samples ($k_I = 0.3$ and $k_{II} = 1.3$), and the same trend was also observed in three-point bending tests (see Section S4, Supplementary Information). Note that the gauge factors k_I and k_{II} signify sensitivity to elastic deformation and sensitivity to inelastic deformation and damage, respectively [41], and were comparable, in magnitude, to those of other types of nanocomposites reported in the literature (see Table S5, Supplementary Information). In the U-0.5 composite, the MWCNTs are more sparsely distributed due to which the morphology of the conductive network changes swiftly through mechanisms such as tunneling, changes in contact resistance between MWCNTs and destruction of conductive networks under tensile loading, resulting in a higher sensitivity to the applied strain [36, 38]. In comparison, both U-0.5 and U-1 showed lower sensitivity in the linear-elastic regime than in the inelastic regime.

3.4. Mechanical and piezoresistive response of MWCNT/UHMWPE lattice structures

To identify an optimal set of process parameters for printing the 2D lattice structures, several test prints were executed with the U-0.5 composite powder in which the laser power was varied between 4.2 and 8.4 W, while all other process parameters were chosen as listed in the Supplementary Table S1. In Fig. S8 (Supplementary Information) we present photographs and μCT images of the 3D printed samples for different choices of laser power. It can be seen that the samples printed at higher laser powers (i-e, 7 W and 8.4 W) showed poor dimensional accuracy (i.e. thickened struts) due to sintering of non-laser irradiated powder on the print bed. In contrast, the samples printed at the lowest laser power (4.2 W) was found to be fragile due to their high level of porosity (~8%), as observed form μCT images (see Fig. S8). Keeping this in view, we selected a laser power of 5.6 W for printing the 2D lattice structures examined herein.

3.4.1. Tensile response of 2D hexagonal lattice structures

Fig. 6a presents the uniaxial tensile stress–strain response along with the corresponding piezoresistance measurements for a 2D hexagonal lattice structure printed using the U-0.5 powder. Here, stress is defined as the average engineering stress induced in the lattice structure, and was calculated by dividing the applied force with the effective cross-sectional area (45 × 3 mm^2). The structure failed in a brittle manner at $\varepsilon = 6.6$ % due to fracture of the struts near the nodes, as seen from the inset of Fig. 6a and Video SV1 (Supplementary Information). Regarding the piezoresistive response, the sample exhibited an almost linear increase in $\Delta R/R_0$ with increasing ε, reporting a gauge factor (k), of 1, which lies between the elastic and inelastic gauge factors measured for the parent nanocomposite in uniaxial tension, $k_I = 0.6$ and $k_{II} = 2.6$, respectively. In the hexagonal lattice structure, the MWCNT network experiences non-uniform strains, since the inclined struts undergo a combination of stretching, bending and shearing deformations under an applied tensile load (see schematic diagram in Fig. S12, Supplementary Information). Hence, it is reasonable to expect that both elastic and inelastic zones coexist in these lattice struts during tensile loading, yielding an average gauge factor of $k_1 \leqslant k \leqslant k_{II}$. Further, it is plausible to assume that the relatively thin struts of the 2D lattice structures

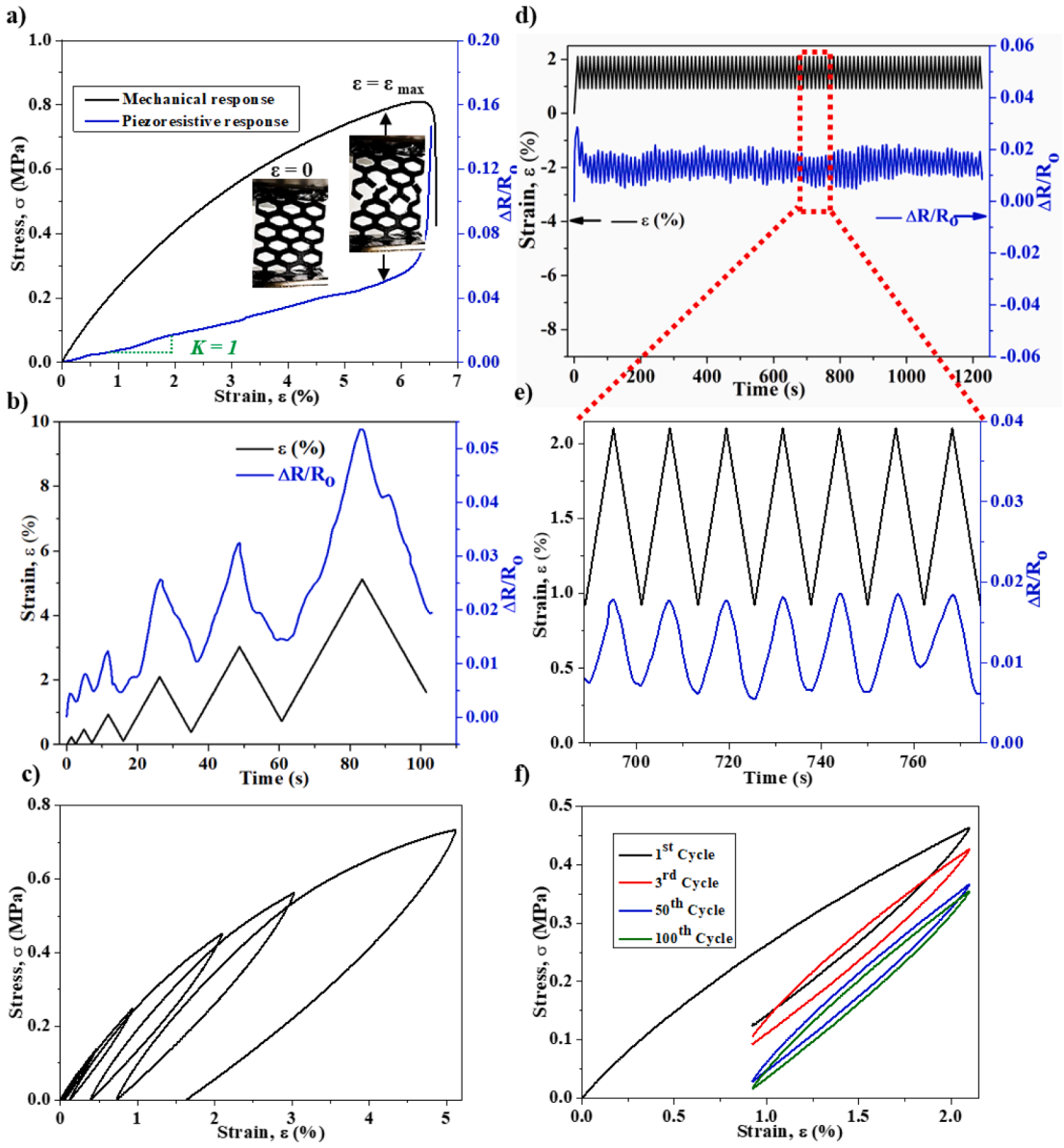

Fig. 6. Mechanical and piezoresistive responses of MWCNT/UHMWPE 2D hexagonal lattice structures (0.5 wt% MWCNTs) under: (a) quasi-static uniaxial tension; (b, c) incremental cyclic loading in tension; (d-f) constant cyclic loading in tension (100 cycles).

experience different thermal histories during 3D printing as they were processed using a laser power of 5.6 W (see Fig. S8) which is different to the laser power used for processing the bulk specimens (printed at 8.4 W, see Table S1), and this may affect the degree of sintering, to some extent, and hence the piezoresistive characteristics of the printed nanocomposite. However, since the differences in the porosities observed in the hexagonal lattice structure (Fig. S8) and the bulk specimens (Fig. 4) were very similar, the difference in the laser power is expected to have insignificant influence on the piezoresistance.

3.4.2. *Cyclic response of 2D hexagonal lattice structures*

In Fig. 6b, we show the time history of the applied strain, ε, together with the corresponding $\Delta R/R_0$ response of the 2D lattice structures (U-0.5; relative density, $\rho = 50\%$) for the case of incremental cyclic loading (see Section 2.5.2); the average stress generated in the lattice structure as a function of imposed strain from the same test is plotted in Fig. 6c. The hysteresis loops observed in the stress–strain response (see Fig. 6c) indicate that energy was dissipated in each of the initial load-unload cycles due to the viscoelastic nature of the UHMWPE matrix (loss factor of U-0.5, $\tan\delta = 0.08$ at room temperature, see Supplementary Fig. S2). In the subsequent cycles, due to increased strain amplitude, the energy was dissipated predominantly via viscoplastic deformation. Note that the residual inelastic strains upon unloading to zero stress, ε_r, increased with increasing strain amplitudes, due to the occurrence of viscoplastic deformation. Moreover, it is seen from Fig. 6b that the measured peaks in the $\Delta R/R_0$ vs. time histories follow similar trends as the maximum strain applied in each cycle. However, we also observe some fluctuations in the recorded $\Delta R/R_0$ signals which can be attributed to configurational changes in the polymer network and the embedded nanofillers that are not fully reversible upon unloading [36]. As shown in the Supplementary Fig. S9, the $\Delta R/R_0$ values measured at the peaks and valleys of the cyclic piezoresistance curve (Fig. 6b), follow similar trends as in the quasi-static tensile test.

In Fig. 6d-f we show the mechanical and piezoresistive responses of the 2D lattice structure (U-0.5) subject to 100 strain-controlled constant amplitude (2%) load cycles. Since the propagation of fatigue cracks was not observed during this test, the mechanical and piezoresistive responses reported in Fig. 6d-f correspond to the viscoelastic deformation

of the 2D lattice structure. Similar to what observed for the case of incremental cyclic loading, the $\Delta R/R_0$ vs. time histories do not exactly follow the same trends as the applied strain histories (see Fig. 6d), particularly during the initial phase of the test where the measured $\Delta R/R_0$ peaks drop significantly over the first four load cycles. As seen from Fig. 6f, the hysteresis loops in the stress–strain response became narrower with time, indicating that less energy was dissipated by viscoelastic deformation as the test proceeded (see Fig. S10, Supplementary Information), resulting in more stable $\Delta R/R_0$ signals. As seen from Fig. 6e, the slopes of the $\Delta R/R_0$ histories are nearly identical during loading and unloading and correspond well with the applied strain histories, suggesting that the MWCNT/UHMWPE lattice structure exhibits good strain sensing performance under cyclic loading conditions.

4. Conclusions

In this study, we experimentally studied the mechanical and piezoresistive characteristics of MWCNT/UHMWPE nanocomposites fabricated via selective laser sintering (SLS) technique. First, the as-received UHMWPE powder was blended with MWCNTs via ball milling and composite powders with 0.3, 0.5 and 1.0 wt% MWCNT loading were synthesized. These powders were then used as the feedstock for SLS 3D printing of electrically conductive MWCNT/UHMWPE composites and 2D lattice structures. The mechanical and piezoresistive characteristics of the 3D printed structures were measured under quasi-static tensile and repeated cyclic loadings, and the underlying structure-processing-property relations were discussed.

It was found that the addition of MWCNTs to UHMWPE improved the elastic modulus and ultimate strength of the sintered parts which was mainly attributable to the reduction in the specimens' porosities, as observed from μCT and SEM images. However, it is believed that the net effect of increase in crystallinity, reduction in porosity and the reinforcing effect due to the addition of MWCNTs govern the macroscopic mechanical properties of composite. Among all compositions considered herein, the MWCNT/UHMWPE composite with 0.5 wt% MWCNT loading had the lowest porosity (~1%) and therefore exhibited superior mechanical properties, reporting a tensile strength of 20.3 MPa which was ~ 51% higher than that of the pure UHMWPE, and ~ 45% above the highest tensile strength reported in the current literature for SLS-printed UHMWPE and UHMWPE-based nanocomposites. The MWCNT/UHMWPE nanocomposite with 0.5 wt% MWNCT loading also outperformed the other compositions in terms of piezoresistive response, showing a gauge factor of 0.6 and 2.6 in the elastic and inelastic regime, respectively. At a higher loading (1 wt%), the MWCNTs formed larger agglomerates in the UHMWPE matrix which deteriorated the mechanical and piezoresistive properties of the nanocomposite.

The MWCNT/UHMWPE composite with 0.5 wt% MWCNT loading was used to print 2D hexagonal lattice structures which showed a nearly linear piezoresistive response with a constant gauge factor of 1. Furthermore, strain-controlled cyclic tests demonstrated that the MWCNT/UHMWPE 2D lattice structure is able to maintain a reliable and stable strain sensing capability over 100 repeated load cycles. The long-term performance and the fatigue behaviour of the nanocomposite is left to a subsequent study. The results suggest that the 3D printed multifunctional UHMWPE-based nanocomposites exhibit desirable attributes relevant to developing self-sensing orthopedic implants and devices.

CRediT authorship contribution statement

Muhammad Umar Azam: Validation, Investigation, Data curation, Writing – original draft, Visualization. **Andreas Schiffer:** Conceptualization, Methodology, Validation, Resources, Writing – review & editing, Supervision, Project administration, Funding acquisition. **S Kumar:** Conceptualization, Methodology, Resources, Writing – review & editing, Supervision, Project administration, Funding acquisition.

Declaration of Competing Interest

The authors declare that they have no known competing financial interests or personal relationships that could have appeared to influence the work reported in this paper.

Data availability

Data will be made available on request.

Acknowledgements

The authors are grateful for the financial support provided by Khalifa University through the Competitive Internal Research Award (CIRA) 2018 [grant number CIRA-2018-128]. Authors would also like to thank Mr. P. George from the Advanced Research and Innovation Center (ARIC) at KU for providing help with the μ-CT analysis.

Appendix A. Supplementary material

Supplementary data to this article can be found online at https://doi.org/10.1016/j.compositesa.2023.107701.

References

[1] Bekas DG, Hou Y, Liu Y, Panesar A. 3D printing to enable multifunctionality in polymer-based composites: A review. Compos Part B Eng 2019;179:107540.
[2] Wang Y, Zhou Y, Lin L, Corker J, Fan M. Overview of 3D additive manufacturing (AM) and corresponding AM composites. Compos Part A Appl Sci Manuf 2020;139:106114.
[3] Schneider J, Kumar S. Multiscale characterization and constitutive parameters identification of polyamide (PA12) processed via selective laser sintering. Polym Test 2020;86:106357.
[4] Goodridge RD, Shofner ML, Hague RJM, McClelland M, Schlea MR, Johnson RB, et al. Processing of a Polyamide-12/carbon nanofibre composite by laser sintering. Polym Test 2011;30:94–100.
[5] Azam MU, Samad MA. UHMWPE hybrid nanocomposite coating reinforced with nanoclay and carbon nanotubes for tribological applications under water with/without abrasives. Tribol Int 2018;124:145–55.
[6] Kurtz SM. UHMWPE Biomaterials Handbook. second edi. Boston: Academic Press; 2009.
[7] Changhui S, Aibing H, Yongqiang Y, Di W, Jia-kuo Y. Customized UHMWPE tibial insert directly fabricated by selective laser sintering. Int J Adv Manuf Technol 2016;85:1217–26.
[8] Dion NT, Bragdon C, Muratoglu O, Freiberg AA. Durability of highly cross-linked polyethylene in total hip and total knee arthroplasty. Orthop Clin North Am 2015;46:321–7.
[9] Reddy SK, Kumar S, Varadarajan KM, Marpu PR, Gupta TK, Choosri M. Strain and damage-sensing performance of biocompatible smart CNT/UHMWPE nanocomposites. Mater Sci Eng C 2018;92:957–68.
[10] Song C, Huang A, Yang Y, Xiao Z, Yu JK. Effect of energy input on the UHMWPE fabricating process by selective laser sintering. Rapid Prototyp J 2017;23:1069–78.
[11] Zhu X, Yang Q. Sintering the feasibility improvement and mechanical property of UHMWPE via selective laser sintering. Plast Rubber Compos 2020;49:116–26.
[12] Rimell JT, Marquis PM. Selective laser sintering of ultra high molecular weight polyethylene for clinical applications. J Biomed Mater Res 2000;53:414–20.
[13] Goodridge RD, Hague RJM, Tuck CJ. An empirical study into laser sintering of ultra-high molecular weight polyethylene (UHMWPE). J Mater Process Technol 2010;210:72–80.
[14] Khalil Y, Kowalski A, Hopkinson N. Influence of energy density on flexural properties of laser-sintered UHMWPE. Addit Manuf 2016;10:67–75.
[15] Khalil Y, Hopkinson N, Kowalski A, Fairclough JPA. Influence of laser power on morphology and properties of laser-sintered UHMWPE. Solid Free Fabr 2016 Proc 27th Annu Int Solid Free Fabr Symp - An Addit Manuf Conf SFF 2016 2016:814–33.
[16] Khalil Y, Kowalski A, Hopkinson N. Influence of laser power on tensile properties and material characteristics of laser-sintered UHMWPE. Manuf Rev 2016;:3.
[17] Shirasu K, Yamamoto G, Hashida T. How do the mechanical properties of carbon nanotubes increase? An experimental evaluation and modeling of the engineering tensile strength of individual carbon nanotubes. Mater Res Express 2019:6.
[18] Kinloch IA, Suhr J, Lou J, Young RJ, Ajayan PM. Composites with carbon nanotubes and graphene: An outlook. Science (80-) 2018;362:547–53.
[19] Ji M, Deng H, Yan D, Li X, Duan L, Fu Q. Selective localization of multi-walled carbon nanotubes in thermoplastic elastomer blends: An effective method for tunable resistivity-strain sensing behavior. Compos Sci Technol 2014;92:16–26.
[20] Li Z, Wang Z, Gan X, Fu D, Fei G, Xia H. Selective laser sintering 3D printing: A way to construct 3D electrically conductive segregated network in polymer matrix. Macromol Mater Eng 2017;302:1–10.

[21] Ronca A, Rollo G, Cerruti P, Fei G, Gan X, Buonocore GG, et al. Selective laser sintering fabricated thermoplastic polyurethane/graphene cellular structures with tailorable properties and high strain sensitivity. Appl Sci 2019;9:1–15.
[22] Qi F, Chen N, Wang Q. Preparation of PA11/BaTiO3 nanocomposite powders with improved processability, dielectric and piezoelectric properties for use in selective laser sintering. Mater Des 2017;131:135–43.
[23] Yazdani B, Chen B, Benedetti L, Davies R, Ghita O, Zhu Y. A new method to prepare composite powders customized for high temperature laser sintering. Compos Sci Technol 2018;167:243–50.
[24] Yuan S, Zheng Y, Chua CK, Yan Q, Zhou K. Electrical and thermal conductivities of MWCNT/polymer composites fabricated by selective laser sintering. Compos Part A Appl Sci Manuf 2018;105:203–13.
[25] Lupone F, Padovano E, Ostrovskaya O, Russo A, Badini C. Innovative approach to the development of conductive hybrid composites for Selective Laser Sintering. Compos Part A Appl Sci Manuf 2021;147:106429.
[26] Song S, Li Y, Wang Q, Zhang C. Boosting piezoelectric performance with a new selective laser sintering 3D printable PVDF/graphene nanocomposite. Compos Part A Appl Sci Manuf 2021;147:106452.
[27] Arif MF, Kumar S, Gupta TK, Varadarajan KM. Strong linear-piezoresistive-response of carbon nanostructures reinforced hyperelastic polymer nanocomposites. Compos Part A Appl Sci Manuf 2018;113:141–9.
[28] Arif MF, Kumar S, Shah T. Tunable morphology and its in fluence on electrical, thermal and mechanical properties of carbon nanostructure-buckypaper. Mater Des 2016;101:236–44.
[29] Yuan S, Chua CK, Zhou K. 3D-printed mechanical metamaterials with high energy absorption. Adv Mater Technol 2019;4:1–9.
[30] Goodridge RD, Tuck CJ, Hague RJM. Laser sintering of polyamides and other polymers. Prog Mater Sci 2012;57:229–67.
[31] Bai J, Goodridge RD, Hague RJM, Song M. Improving the mechanical properties of laser-sintered polyamide 12 through incorporation of carbon nanotubes. Polym Eng Sci 2013;53:1937–46.
[32] Dorigato A, Brugnara M, Pegoretti A. Novel polyamide 12 based nanocomposites for industrial applications. J Polym Res 2017;24:1–13.
[33] Warnakula A, Singamneni S. Selective laser sintering of nano Al2O3 infused polyamide. Materials (Basel) 2017:10.
[34] Maksimkin AV, Kharitonov AP, Mostovaya KS, Kaloshkin SD, Gorshenkov MV, Senatov FS, et al. Bulk oriented nanocomposites of ultrahigh molecular weight polyethylene reinforced with fluorinated multiwalled carbon nanotubes with nanofibrillar structure. Compos Part B Eng 2016;94:292–8.
[35] Bai J, Goodridge RD, Yuan S, Zhou K, Chua CK, Wei J. Thermal influence of CNT on the polyamide 12 nanocomposite for selective laser sintering. Molecules 2015;20:19041–50.
[36] Kumar S, Gupta TK, Varadarajan KM. Strong, stretchable and ultrasensitive MWCNT / TPU nanocomposites for piezoresistive strain sensing. Compos Part B 2019;177:107285.
[37] Mora A, Verma P, Kumar S. Electrical conductivity of CNT/polymer composites: 3D printing, measurements and modeling. Compos Part B Eng 2020;183:107600.
[38] Avilés F, Oliva-Avilés AI, Cen-Puc M. Piezoresistivity, strain, and damage self-sensing of polymer composites filled with carbon nanostructures. Adv Eng Mater 2018;20:1–23.
[39] Verma P, Ubaid J, Varadarajan KM, Wardle BL, Kumar S. Synthesis and characterization of carbon nanotube-doped thermoplastic nanocomposites for the additive manufacturing of self-sensing piezoresistive materials. ACS Appl Mater Interfaces 2022;14:8361–72.
[40] Henry C, Rupel K, Park C, Costanzo J, Kaczowka C. Evaluation of an alternate method for determining yield strength offset values for selective laser sintered polymeric materials. SAMPE 2019 - Charlotte, NC 2019.
[41] Ubaid J, Schneider J, Deshpande VS, Wardle BL, Kumar S. Multifunctionality of nanoengineered self-sensing lattices enabled by additive manufacturing. Adv Eng Mater 2022:24.